AD-A169 116 NUMERICAL SIMULATION OF TIP VORTICES OF WINGS IN SUBSONIC AND TRANSONIC FLOWS(U) JAI ASSOCIATES INC MOUNTAIN VIEW CA G R SRINIVASAN ET AL. 1986 1/1

UNCLASSIFIED ARO-21731.1-EG DAAG29-85-C-0002 F/G 20/4 NL

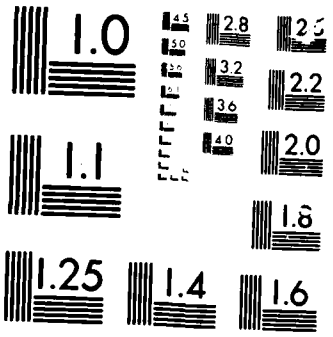

(2)

UNCLASSIFIED
SECURITY CLASSIFICATION OF THIS PAGE (When Data Entered)

MASTER COPY - FOR REPRODUCTION PURPOSES

REPORT DOCUMENTATION PAGE

READ INSTRUCTIONS BEFORE COMPLETING FORM

1. REPORT NUMBER	2. GOVT ACCESSION NO.	3. RECIPIENT'S CATALOG NUMBER
ARO 21731.1-EG	N/A	N/A

4. TITLE (and Subtitle)
Numerical Simulation of Tip Vortices of Wings in Subsonic and Transonic Flows

5. TYPE OF REPORT & PERIOD COVERED
Reprint

6. PERFORMING ORG. REPORT NUMBER

7. AUTHOR(s)
G. R. Srinivasan, W. J. McCroskey, J. D. Baeder & T. A. Edwards

8. CONTRACT OR GRANT NUMBER(s)
DAAG29-85-C-0002

9. PERFORMING ORGANIZATION NAME AND ADDRESS
JAI Associates, Inc
P. O. Box 293
Mountain View, California 94042

10. PROGRAM ELEMENT, PROJECT, TASK AREA & WORK UNIT NUMBERS

11. CONTROLLING OFFICE NAME AND ADDRESS
U. S. Army Research Office
Post Office Box 12211
Research Triangle Park, NC 27709

12. REPORT DATE

13. NUMBER OF PAGES

14. MONITORING AGENCY NAME & ADDRESS (if different from Controlling Office)

15. SECURITY CLASS. (of this report)
Unclassified

15a. DECLASSIFICATION DOWNGRADING SCHEDULE

16. DISTRIBUTION STATEMENT (of this Report)
Approved for public release; distribution unlimited.

17. DISTRIBUTION STATEMENT (of the abstract entered in Block 20, if different from Report)
NA

"Original contains color plates: All DTIC reproductions will be in black and white"

18. SUPPLEMENTARY NOTES
The view, opinions, and/or findings contained in this report are those of the author(s) and should not be construed as an official Department of the Army position, policy, or decision, unless so designated by other documentation.

19. KEY WORDS (Continue on reverse side if necessary and identify by block number)
Subsonic Flow, Transonic Flow, Tip Vortex, Vorticity, Navier-Stokes, Euler

20. ABSTRACT (Continue on reverse side if necessary and identify by block number)
The formation and roll-up process of the tip vortices of wings in subsonic and transonic flows is numerically simulated using a hybrid scheme of solving a zonal algorithm for thin layer Navier-Stokes/Euler eqations. The results are in good agreement with the available limited experimental data including the tip vortex strength.

DD FORM 1 JAN 73 1473 EDITION OF 1 NOV 65 IS OBSOLETE

UNCLASSIFIED
SECURITY CLASSIFICATION OF THIS PAGE (When Data Entered)

AIAA'86

AIAA-86-1095

Numerical Simulation of Tip Vortices of Wings in Subsonic and Transonic Flows

G.R. Srinivasan, JAI Associates, Inc.,
Mountain View, CA
W.J. McCroskey, J.D. Baeder and T.A. Edwards,
NASA Ames Research Center,
Moffett Field, CA

AIAA/ASME 4th Fluid Mechanics, Plasma Dynamics and Lasers Conference
May 12-14, 1986/Atlanta, GA

NUMERICAL SIMULATION OF TIP VORTICES OF WINGS IN SUBSONIC AND TRANSONIC FLOWS

G. R. Srinivasan*
JAI Associates Inc, Mountain View, California

W. J. McCroskey**, J. D. Baeder†
U.S. Army Aeroflightdynamics Directorate - AVSCOM
NASA Ames Research Center, Moffett Field, California

and

T. A. Edwards†
NASA Ames Research Center, Moffett Field, California

Abstract

A multi block zonal algorithm which solves the thin-layer Navier-Stokes and the Euler equations is used to numerically simulate the formation and roll-up of the tip vortex in both subsonic and transonic flows. Four test cases which used small and large aspect ratio wings have been considered to examine the influence of the tip-cap shape, the tip-planform and the free-stream Mach number. It appears that both the tip-planform and the tip-cap shape have some influence on the formation of the tip vortex, but its subsequent roll-up seems to be more influenced by the tip-planform shape. In general, a good definition of the formation and the roll-up of the tip vortex has been observed for all the cases considered here. Comparisons of the numerical results with the limited, available experimental data show good agreement with both the surface pressures and the tip-vortex strength.

Nomenclature

B	=	semi span of the wing
C	=	root chord of the wing
C_D	=	drag coefficient
C_L	=	lift coefficient
C_M	=	quarter-chord, pitching-moment coefficent
C_P	=	pressure coefficient
$\hat{E}, \hat{F}, \hat{G}$	=	flux vectors
M_∞	=	free-stream Mach number
$\hat{Q}$	=	flow-field vector
$\vec{q}$	=	velocity vector
Re	=	Reynolds number
$\hat{S}$	=	viscous flux vector
u_∞	=	free-stream velocity
X, Y, Z	=	Cartesian coordinates
α	=	angle of attack, degrees
Γ_V	=	dimensionless strength of tip vortex
ξ, η, ζ, τ	=	generalized curvilinear coordinates

Introduction

The phenomenon of formation and subsequent roll-up of tip vortices behind finite aspect-ratio wings has long attracted a great amount of attention because of their potential hazard to aircraft that encounter them in flight. To date there are many theoretical, numerical, and experimental studies in the literature which are devoted entirely to the understanding of such flows encompassing large aircraft wakes (see for example Refs. 1-2). In spite of this, the present understanding of such flows remains essentially qualitative. In all these studies, the detailed knowledge of the mechanics of the formation and subsequent roll-up of tip vortices have been precluded. In addition to the fixed-wing aircraft, the operating characteristics of helicopters are strongly influenced by the vortex wakes of the rotating blades. The dominant feature of such wakes is the helical vortices which have their origin at the tips of the rotor blades. The interaction of these blades with the vortex wake changes their aerodynamic loads and thus affects their operating performance, vibration, and acoustic characteristics. Although a detailed knowledge of the formation and the initial roll-up of such concentrated vortices is not used for typical current wake analyses, such a knowledge is essential to modify the structure of these vortices and to minimize their influence. Thus, it is important to study in detail the flow field in the vicinity of the tip of a finite wing and of a helicopter rotor blade. In addition, the recent interest in the generation of high lift coefficients for V/STOL operations has spurred further increased interest in understanding the physics of the formation of tip vortices and their subsequent downstream trajectories.

The typical flow field in the tip region of a finite aspect ratio wing is strongly three-dimensional and often is separated. Vortex filaments shed in this region, from the viscous layer near the surface, interact with each other to form a

* Senior Research Scientist, Member AIAA
** Senior Staff Scientist, Associate Fellow AIAA
† Research Scientist, Member AIAA

discrete tip vortex whose strength and size are dictated by the aerodynamic and geometrical constraints of the wing and of the wing tip-geometry respectively. In most prediction schemes, the true physical situation is related to an analytical model through the concept of bound vorticity. In reality, the bound vorticity is that which is continually generated as a result of the viscous nature of the boundary layer near the wing surface and which appears to be attached to the wing tip in the Eulerian reference frame (Ref. 3).

Therefore it appears that the formation of the vortex originating from round edges is a viscous phenomenon. However, the recent works of Rizzi et al. (Ref. 4) and of Mitchelltree et al. (Ref. 5) have used Euler equations to numerically simulate the vortex formation and its subsequent roll-up. The reason for the success of such a procedure is that the artificial viscosity, used in the numerical scheme to control the nonlinear stability, has played the role of the natural viscosity. More recently, in a pioneering, but limited work, Mansour (Ref. 6) used the thin-layer Navier-stokes equations (Ref. 7), in conjunction with an elliptic grid generation scheme, to simulate the flow field and the tip-vortex of a low-aspect-ratio wing. In spite of a clever data management strategy, the central processing unit (CPU) time for each steady-state calculation exceeded 25 hours on NASA Ames CRAY 1-S machine, with only 75,000 grid points in the entire flow field, for a five-order-of-magnitude drop in the residuals. In the present work an attenuate but more efficient method of multi block zonal approach (Refs. 8,9) is used to simulate the flow fields of isolated wing sections by solving the Euler thin-layer Navier-Stokes equations with a view to simulating the tip-vortex formation in subsonic and transonic flows.

At the Reynolds numbers of interest for the present calculations, the flow around the wing can be considered to be *mostly inviscid except in a small, but crucial, region near* the body surface where the viscous effects are important. Accordingly, the flow field is solved using a multi block zonal approach developed at NASA Ames Research Center (Refs. 8,9) wherein the inviscid outer blocks are solved using the Euler equations and the inner viscous blocks are solved using the thin-layer Navier-Stokes equations. The results of wing flow topology and of the tip-vortex are presented for four different wing shapes, with three of them being in transonic flow and one in subsonic flow. The influences of the tip-planform and of the tip-cap effect on the tip-vortex formation are also discussed. In addition, the results from the multi block zonal approach are compared with the results from a one-block solution of thin-layer Navier-stokes equations. The numerical results are compared with the limited available experimental data.

Governing Equations and Numerical Scheme

The governing partial differential equations are the thin-layer Navier-Stokes and the Euler equations (Refs. 7,10). The equations are generally nondimensionalized by free-stream quantities and are transformed to the arbitrary curvilinear space (ξ, η, ζ, τ) while retaining strong conservation law form to capture shock waves. The transformed equations written in generalized curvilinear coordinates are given by (Refs. 7,10)

$$\partial_\tau \hat{Q} + \partial_\xi \hat{E} + \partial_\eta \hat{F} + \partial_\zeta \hat{G} = \epsilon Re^{-1} \partial_\zeta \hat{S} \qquad (1)$$

where

$$\hat{Q} = J^{-1} \begin{bmatrix} \rho \\ \rho u \\ \rho v \\ \rho w \\ e \end{bmatrix}, \quad \hat{E} = J^{-1} \begin{bmatrix} \rho U \\ \rho u U + \xi_x p \\ \rho v U + \xi_y p \\ \rho w U + \xi_z p \\ U(e+p) - \xi_t p \end{bmatrix}$$

$$\hat{F} = J^{-1} \begin{bmatrix} \rho V \\ \rho u V + \eta_x p \\ \rho v V + \eta_y p \\ \rho w V + \eta_z p \\ V(e+p) - \eta_t p \end{bmatrix}, \quad \hat{G} = J^{-1} \begin{bmatrix} \rho W \\ \rho u W + \zeta_x p \\ \rho v W + \zeta_y p \\ \rho w W + \zeta_z p \\ W(e+p) - \zeta_t p \end{bmatrix} \qquad (2)$$

and $\epsilon = 0$ for Euler equations, and $\epsilon = 1$ for thin-layer Navier-Stokes equations. The viscous flux vector $\hat{S}$, in the thin-layer approximation, is given in Ref's. 7 and 10. The primitive variables of Eq. (1), viz., $\rho, \rho u, \rho v, \rho w$ and e are normalized by the free-stream reference quantities. The relations for the contravariant velocities U, V and W, the Jacobian of transformation J, and the metric are described in Refs. 7 and 10.

The velocity components u, v, w and the pressure, p, are related to the total energy per unit volume, e, through the equation of state for a perfect gas by

$$p = (\gamma - 1)\left(e - \frac{\rho}{2}(u^2 + v^2 + w^2)\right) \qquad (3)$$

The numerical code which solves these equations, called ARC3D (Refs. 10), was adapted by Holst et al. (Ref. 8) and Flores (Ref. 9) to develop the transonic Navier-Stokes (TNS) multi block zonal algorithm. Most of the important features of the ARC3D code are contained in the TNS code with one important difference, viz., when dealing with multiple blocks. The development of this 4-block version of the TNS code and the improvements to the numerical algorithm to handle multiple zones or blocks are described

in detail in the papers of Holst et al. (Ref. 8) and of Flores (Ref. 9). In addition to the example solutions for isolated wings discussed in these two papers, Kaynak et al. (Ref. 11) report further refinements to this code to analyze large-scale separation on wings. The present version of this 4-block scheme is mainly used for computing isolated wing solutions, with or without wind-tunnel walls. However, a 16-block version of this code for simulating the complete flow field of a fighter aircraft is currently under development.

There are five important features of the TNS code. (1) The thin-layer Navier-Stokes equations and the Euler equations are solved in strong conservation-law form to capture the shock waves. (2) The convergence procedure is significantly accelerated over the standard ARC3D code (Ref. 10), which solves thin-layer Navier-Stokes equations over the complete flow domain, because the present scheme solves the Euler equations over a significant part of the flow domain. (3) There are two numerical options for solving the equations. One is based on the ADI algorithm which solves block-tridiagonal matrices along each coordinate direction (Ref. 12). The other is based on the diagonalized algorithm (Ref. 13) which solves a set of five scalar pentadiagonal matrices along each coordinate direction. (4) The diagonal algorithm has been implemented with two options of variable time-step philosophies to accelerate the convergence rate of the numerical scheme, viz., one that scales the marching time-step with the transformation Jacobian (Ref. 14) and the other that scales the time-step using a combination of the Jacobian and local solution variation (Ref. 9,10). (5) The code is vectorized for the CRAY-XMP machine.

Both numerical schemes (TNS and ARC3D) use the standard second-order-accurate central differencing to construct the appropriate spatial differencing scheme. The diagonal scheme, which is used in the present study to calculate steady-state solutions, uses fourth-order-accurate smoothing operators on the implicit and explicit sides of the numerical algorithm for controlling nonlinear stability of the numerical scheme. In the present calculations a turbulent boundary layer is assumed for the entire wing, and the Baldwin and Lomax algebraic turbulence model (Ref. 14), which is currently available in the TNS code, is used to calculate the turbulent eddy viscosity.

Grid Generation and Data Management

The details of the grid generation scheme and the data management system are described in Ref. 8. For the sake of completeness, the important steps that are necessary to generate a working finite-difference grid are described. First, a coarse grid encompassing the entire flow field is generated using the patatoric grid-generation scheme of Eiseman (Ref. 15). The grid has an H-grid topology in the spanwise and chordwise directions. This grid is then split into several blocks or zones by means of the zoning algorithm in the TNS code. Thus the complete flow domain is divided into four blocks. Figure 1 shows one such grid topology for the Wing C section. In this view, the grid at the symmetry plane of the wing is shown. The coarse (inviscid) outer grid, marked as block (1), is shown in white, the finer inviscid grid, marked as block (2), is shown in red. The two-blocks adjacent to the wing and on either side of it, marked as blocks (3) and (4) are shown in yellow, and are the viscous blocks which have clustering in the leading-edge and trailing-edge regions as well as in the wing tip region which is used to resolve the tip vortex. The inviscid grids also have clustering as shown.

In the present case, each of the four zones typically has over 40,000 grid points. Although the grid geometry for each wing discussed here depended on the aspect ratio of the individual wing, the spanwise grid spacing at the wing tip and the spacing in the normal direction to the wing surface, which were used to resolve the boundary layer, were kept same for all the wings, viz., 0.015 of chord and 1×10^{-5} of chord, respectively. The viscous blocks had 25 grid points in the normal direction for all the wings.

The data managemant strategy is discussed by Holst et al. (Ref. 8) and also by Kaynak et al. (Ref. 11). In brief, the base grid, usually generated outside the TNS code, is "read in" first and this grid is divided into the proper zones by the "Zoner" code. Once this is done, the flow solver is initiated. The iteration procedure starts in the outer inviscid zone or block, and proceeds into the inner viscous blocks. The information necessary to update the boundary conditions at the zonal interface is found from the neighboring zones through a series of one-dimensional linear interpolations. Such a scheme lends itself to a conservative treatment of the boundaries and thus captures distortion-free-movement of discontinuities across the boundaries.

In the solution procedure, only the information necessary to solve each zone resides at any one time in the main memory of the CRAY-XMP computer. The information of zones which are not being computed is stored temporarily on the solid state device (SSD). The use of SSD allows a great deal of flexibility and thus frees the main memory of the space normally taken by the data stored on the SSD and enables the use of maximum number of grid points in the flow field. Also, the use of SSD reduces the I/O wait time significantly (Ref. 9).

Boundary Conditions

Since the TNS code is a multi zonal algorithm, there are two types of boundaries where conditions have to be specified: viz., (1) the physical boundaries such as inflow, outflow, and the surface conditions; and (2) the zonal boundaries where all the flow quantities have to be made continuous. All the boundary and interface or zonal conditions used are applied explicitly.

At the far-field boundaries, which are 6-10 chords away from the wing, free-stream values are specified for all the flow quantities. At the outflow boundaries, zeroth-order extrapolation is used from the grid interior. At the symmetry plane, a zeroth-order extrapolation is used for the density and a first-order extrapolation is used for the x-component and the z-component of velocities while setting

the spanwise velocity component to zero to force symmetry. A first-order extrapolation is also used for the pressure and the energy is calculated from the equation of state. At the surface of the wing, a no-slip condition is used for the three velocity components and the pressure is calculated by solving the normal momentum equation at the surface. In the spirit of the thin-layer approximation, the normal momentum equation would translate into $dp/dn = 0$, where n is the local normal to the surface. Density is determined by assuming adiabatic wall conditions. Having known the pressure, p, and density, ρ, at the wall, the total energy, e, is determined from Eq. (3). The details of the interface boundary conditions at the zone interfaces are described in Refs. 8 and 11.

Results and Discussion

In this section, numerical results for flow fields and tip-vortex formation are presented for four different wing sections. These results are compared with the available experimental data. The different flow conditions and the wing geometries considered consist of: (1) a rectangular wing with an aspect ratio of 2.5 without twist or taper, in a uniform flow of $M_\infty = 0.16$ and at 11 degrees angle of attack; (2) a wing with a small aspect ratio of 0.83 with twist and taper in a uniform flow of $M_\infty = 0.9$ and at 5 degrees angle of attack; and (3) two wings with exotic tip shapes, both having an aspect ratio of 5.0, in a uniform flow of $M_\infty = 0.85$ and at 5 degrees angle of attack. The planforms and the fine surface grid (at every grid point) for these different wing geometries are shown in Fig. 2. The boundary layer is assumed to be turbulent for the entire wing sections.

Rectangular Wing in Subsonic Flow

This wing consists of a rectangular wing with a square tip and is made up of NACA-0015 airfoil sections without twist or taper. Its planform and surface grid are shown in Fig. 2a. For this wing in a uniform free-stream of $M_\infty = 0.16$ and at 11 degrees angle of attack, the steady-state flow field was calculated using the TNS code. The flow Reynolds number, based on the free-stream velocity and the chord of the wing, was 2 million. Typical computational time, for a four-order drop in residuals, was of the order of 3 hours on the CRAY-XMP machine.

The steady-state results for this wing are shown in Figs. 3-6. Figure 3 shows the computed surface pressure distributions at several spanwise stations compared with the experimental data of Spivey and Moorhouse (Refs. 16,17). The inboard spanwise stations show good agreement with the experiments as seen in Figs. 3a-3c. However, the suction peak associated with the tip vortex that was observed at the 97% spanwise station near the trailing edge region, as shown in Fig. 3d, has not been well predicted. The probable reason for this can be explained by examining the tip-cap profile of the present wing goemetry. The top half of Fig. 4 shows the details of the tip-cap at the X = 50% station. This tip-cap, although it resembles a circular cap at this X-station, it has a very different shape at other stream wise stations. A detailed examination of the tip-cap profile at other streamwise stations, shown for example for X = 75% and for X = 90% in Fig. 4, indicates that its shape changes in the leading- and trailing-edge regions to that of a sharp corner. This sharp corner at the leading-edge apparently may be responsible for producing a larger separation than a square-tip wing would produce and thus nullifying the suction peak associated with the tip vortex. The calculated pressure field agrees with the experiment at this 97% spanwise station on the lower surface and on most of the upper surface, except for the important suction peak near the trailing-edge region.

To examine further the influence of the tip-cap shape on the flow field in the tip region, the rectangular wing with square tip was modified by adding an ellipsoidal tip-cap that produces a smooth, rounded surface along the tip. This cap has a minor axis equal to half the thickness of the wing. In order to represent this smooth curved tip, the surface grid resolution was increased to twice the value in the spanwise direction to that used earlier. The tip of the wing with this tip-cap is rounded off in all the directions to avoid sharp corners. The finite difference grid for this wing consists of a spherically warped grid of O-O topology generated by the hyperbolic grid solver of Steger and Chaussee (Ref. 18), and is shown in Fig. 4 at the X = 50% streamwise station.

To generate the steady-state solution for this wing at the same flow conditions of $M_\infty = 0.16$, $\alpha = 11$ degrees, and Re = 2 million, a single-block, thin-layer Navier-Stokes flow solver called PEN3D (Ref. 19) is used. This code is also a derivative of the ARC3D code (Ref. 10) but is coded in the VECTORAL language. The essential details of this code are described in Pan and Pulliam's paper (Ref. 19). All the features of this code are identical to the TNS code but it is limited to applications with only single-block grids. The present single- block grid has the dimensions of 110 points in the periodic direction, 44 in the spanwise direction, and 66 in the normal direction.

Typical results of the steady-state solution for this wing are shown in Figs. 3c-d in the form of surface-pressure distributions. The results agree well with the TNS calculations and the experimental data of Spivey and Moorhouse (Refs. 16,17) from the wing root to the 90% spanwise station. Although the PEN3D calculations show a suction peak in the tip region, because of the formation of the vortex, it is not as large as that observed in the experiment.

This rounded tip-cap did not produce any separation in the tip region on the upper surface of the wing, as seen from the surface oil picture of Fig. 5a. (The surface oil flow picture is generated by releasing fictitious fluid particles at one grid point above the surface and by restricting these particles to that plane.) In contrast, the tip-cap shape discussed earlier produces large separation in the tip region for this wing as shown in the surface oil flow picture of Fig. 6. The extent of the separation region on this wing is more pronounced than is apparent from the pressure contour plot of Chigier and Corsiglia (Ref. 20) indicating that the tip-cap of Fig. 4a top view, first thought to mimic the experimental

square tip, is really different and is neither a near-square nor a near-rounded tip. The sharp corner at the leading edge in the tip seems to be separating the flow at this point as seen from the close-up view of surface oil picture of Fig. 7a.

The close-up views of the lift-off of the tip vortex for these two tips are shown in Figs. 5b and 7b. The tip vortex for the rounded tip wing of Fig. 5a is lifting off from the tip-face well before the trailing edge. For the non-rounded tip of Fig. 7b, the tip vortex is lifting off from the upper surface of the wing at about the trailing edge position. Both the tip shapes of Figs. 5b and 7b show the three-dimensional trajectories of the particles around the tip. The particles released on the lower surface of the wing cross over the tip region into the low-pressure region of the upper surface of the wing. These particles mix with the particles released on the upper surface and together they define a tip vortex that is distinct from the rest of the sheet. The tip vortex then rolls up, slightly inboard of the wing tip, as it leaves the wing surface (Fig. 5b). Further downstream of this, the tip vortex rolls inboard and stays distinctly above the shed vortex sheet as seen in the far-field view of the tip vortex shown in Fig. 8. Also, shown in Fig. 8 are the vorticity contours in the Y-Z planes through the tip vortex at several downstream X-locations. In this figure, the magnitude of the vortex contour increases in the order of the change in color according to the blue-green-yellow-red. Judging from the magnitudes of the contours, the core vorticity is maximum when it is just downstream of the trailing edge of the wing. However, at the downstream grid boundary, which is 6 chords away from the wing, the vorticity levels have reduced by an order-of-magnitude caused by a very coarse grid structure. It is also interesting to see that the vortex structure in the far-field is stretched in accordance with the local grid shape. Close to the wing, the structure is somewhat axisymmetric and as the grid gets coarser in block 1, the vortex shape gets stretched accordingly.

The lift, drag, and quarter-chord pitching-moment coefficients calculated from the TNS code for this wing are 0.702, 0.0748, and -0.00976 respectively. This compares well with the measured values of 0.763, 0.0868, and -0.00843 for the lift, drag, and pitching-moment coefficients, respectively, at α 12 degrees.[1] The lift per degree of angle of attack , C_L α, for both the experiment and the TNS calculations is approximately 0.064 degree. The modified tip with PEN3D gave a value of 0.07 degree. From this the approximate strength of tip vortex, using the definition of lift equivalent vortex strength, is 0.35. (Note the vortex strength quoted here is a dimensionless quantity, nondimensionlized by the free-stream velocity and by the chord of the wing.) Another method of evaluating the tip vortex strength is by doing a line integral of the velocity vector over a closed path enclosing the vortex, viz.,

$$\Gamma_V \quad \int_S q \cdot ds \qquad (4)$$

[1]Tabulated data from experiments of Spivey and Moorhouse (Refs 16,17) provided by U. S. Army Aeroflightdynamics Directorate

The result of such a line-integral at several X-stations behind the wing over a path big enough to enclose the vortex gave a range of values from 0.33-0.38, depending on the size of the integration path around the vortex. The larger value corresponds to the case of line-integral path exending all the way to the wing root in the Y-direction and extending to the limits in Z-direction. This path will include the contribution from the vortex sheet in the wake also. The tip vortex strength from these two methods is estimated to be 0.35.

Wing C in Transonic Flow

WING C belongs to the class of advanced technology wing sections and has been extensively studied both computationally (Refs. 6,11) and in wind-tunnel experiments (Refs. 21,22). Its planform and the surface grid are shown in Fig. 2b. It is a low-aspect-ratio wing (0.83 based on the root chord) which is made of supercritical wing sections, with a twist angle of 8.17 degrees, a taper ratio of 0.3 and a leading- edge sweep of 45 degrees. Recently Kaynak et al. (Ref. 11) have presented extensive computational results for this wing for a range of Mach numbers. These results were also computed using the TNS code. Whereas this study concentrated on analysing the flow topology, the present study specializes in the flow in the vicinity of the wing tip and in particular concentrates on the tip vortex phenomenon. As noted earlier, Mansour (Ref. 6), in a pioneering but limited study, attempted to simulate the tip vortex formation for this wing in a free-stream Mach number of 0.82 and at 5 degrees angle of attack.

The flow conditions for the present computations are M_∞ 0.9, α 5, and Re 6.8 million based on the mean aerodynamic chord. As before, the baseline coarse grid was generated by the parabolic grid solver of Edwards (Ref. 15) with sufficient grid resolution in the wing tip region so as to resolve the tip vortex. The interior grids are generated within the TNS code by the Zoner program. The CPU time for a fully converged solution was about 3 hours for this case which is highly transonic and has a shock-induced flow separation on the upper surface of the wing.

The calculated surface pressure distributions for several spanwise stations are shown in Fig. 9 and are compared with the experimental data of Keener (Ref. 21). The results show good agreement with the experiments over the parts of the wing which do not have massive shock-induced separation. However, the shock wave position and post-shock pressure levels are not well predicted at the 90% span station. Similar results were obtained by Kaynak et al. (Ref. 11), who discuss the possible reasons for this, including inadequate grid resolution, artificial dissipation, and turbulence model. The other features of the flow are the presence of a strong shock wave in the leading -edge region extending all the way into the inboard of the tip region. Here it coalesces with the secondary shock. This combined shock produces large boundary-layer separation. Figures 10a-b show this shock at 90% spanwise station, and the extent of separation is shown in Fig. 10c. This figure is generated by releasing the fluid particles at one grid point above the

surface and by not restricting them to any surface. The curling of the fluid particles in the separated region indicates the presence of vortical flow. Figures 11-12 show for the upper surface of the wing the surface oil flow pattern and the velocity vector plot. (Just as in the surface oil picture, the velocity vector plot is generated by releasing particles at one grid point above the surface). Both these figures clearly show the extent of separation.

Tip-vortex formation was visualized by releasing several particles at different locations along the span and various heights from the wing surface. Figures 11-12 show the close-up and far-field view of the tip vortex. Because of the large cross flow caused by the high sweep angle, the boundary layer in the tip region becomes thicker. This thick boundary layer easily separates in the presence of the shock wave. Part of this separated flow lifts up from the wing surface and merges into the flow in the tip region. These fluid particles get entangled with the particles coming over the tip from the high-pressure region of the wing's lower surface and in combination these particles separate into the tip vortex, and are distinct from the rest of the vortex sheet. This action is apparent from the picture of Fig. 13 which shows the close-up view of the formation process of the tip vortex. The lift-up of the tip vortex from the surface is apparent in this view. Figure 14 shows the far-field view of the same vortex . This view shows how the tip vortex rolls inboard in the downstream wake. The vorticity contours in the Y-Z planes at several X-locations are seen in Fig. 14. As noted before, the magnitude of vorticity decreases in the far-field coarse grid. But the line-integral of the velocity vector around a closed path surrounding the tip vortex would give the same value for the strength of vortex as long as the integration path was large. For this wing, the calculated values of the aerodynamic coefficients were C_L 0.361, C_D 0.0347, and C_M -0.146. The strength of the vortex determined from the line-integral method yielded a value between 0.17 and 0.185, depending on the size of the integration path around the tip vortex. The smaller value includes the vortex sheet in the wake and therefore corresponds to the larger path of the integral (usually extending to the symmetry plane in the Y-direction and limits of Z in the Z-direction. This implies that the tip vortex strength is equal to 0.185 (normalized by the free-stream velocity and the root chord of the wing).

ONERA Wing in Transonic Flow

This wing has an aspect-ratio of 5 and represents a typical helicopter rotor blade. The tip of the wing is more exotic than are the tips of the two previous wings. The wing is made up of three special airfoil sections ranging in thickness from 12 to 6 %, the thicker section being at the root and the thinnest one at the tip. The wing has a constant chord up to about 70% of the spanwise station and then decreases in the ratio of the thickness ratio. Considering that we can have only 23 points on the wing in the spanwise direction (limited by the memory of the CRAY-XMP) in the fine Euler and the viscous grids, the same number of points as we had for the WING C, the spanwise grid distribution will be very sparse for this wing. Figure 2c shows the planform and the surface grid for this wing. For this wing in a uniform free-stream of M_∞ = 0.85, α = 5 degrees and Re 8.5 million (based on the root chord), computations were carried out to generate a steady-state solution.

Figure 15 shows the computed surface-pressure distibutions for several spanwise stations along the wing. Examination of the pressure distributions indicate the presence of two shock waves, a weak leading-edge shock, and a strong shock downstream of this. The Mach number contour plots of Fig. 16 confirm this. (The Mach number contours were drawn at a plane outside the viscous region.) The main shock extends all the way to the root of the wing which is a symmetry plane. This shock produces large scale separation on the wing. The surface oil flow pattern of Fig. 17 shows the separation and reattachment lines along with other flow features clearly. The shock becomes weak towards the wing tip and the flow gets complicated between the 75% and 90% spanwise stations. An outward spiralling vortex emanates from the separated flow in this region.

Figures 18-19 shows two views of the tip vortex for this wing. The initial formation of the vortex and lifting off from the wing surface is shown in Fig. 18. It appears that the swept-back tip has similar influence as the sweep effect (see Wing C results above), viz., the cross flow and tip-loading influence. This cross flow enables the fluid particles released in the vicinity of the tip to first braid and then to roll-up and lift off from the surface. Also, the fluid particles released on the high-pressure side of the wing (lower surface) at the tip, cross over to the low-pressure side (upper side) by wrapping around the wing tip in the classical three-dimensional tip-relief fashion and braid in to the swirling tip vortex. Figure 19 shows the far-field view of this tip vortex. The lift off of the tip vortex from the wing surface and then the roll inboard in the downstream wake are clearly evident from this photograph. Also, shown in this are vorticity contours drawn in the Y-Z planes through the tip vortex at several X-locations behind the wing. As observed before, the vorticity levels of the contours decrease in the downstream coarse-grid region of Block 1, and the shapes of these contours get stretched in the pattern of the grid geometry.

The lift, drag, and the pitching-moment coefficients for this wing are C_L 0.26, C_D 0.061, and C_M 0.002. Note that the pitching-moment is positive (destabilizing) for this wing. Based on the definition of lift-equivalent vortex strength, the nondimensional tip vortex strength is 0.13. Also, the value of Γ_V determined from the line-integral of the velocity vector around a closed path surrounding the vortex and at several X-locations in the wake lies in the range between 0.12 - 0.14 depending on the path of the integral. The larger value corresponds to the the smaller integral path surrounding the tip vortex. The smaller value includes the effect of wake vortex sheet. From this calculation it can be concluded that the tip vortex strength is 0.14

Effect of Tip Planform

To study the influence of the tip geometry on the tip-vortex formation, the ONERA wing of Fig. 2c was modified to reshape the planform in the tip region, keeping the rest of the geometry the same. The planform and the surface grid for this modified wing is shown in Fig. 2d. This modified wing geometry has an unswept leading edge and looks more like a rectangular wing except the tip region retains the original taper. The flow conditions are kept identical to the case of ONERA wing of section (c) above. Steady-state solution was generated as before using the TNS code for this wing section. From this, the lift, drag, and the pitching-moment coefficients for this wing are C_L = 0.332, C_D = 0.0796, and C_M = -0.018. The obvious gross changes in flow features are the increase in the lift and drag values, and the pitching moment is negative (stabilizing) in constrast to the positive value for the ONERA wing.

The Mach number contour plot of Fig. 20 shows a shock pattern on the surface for this wing, which is swept forward near the tip, and this shock wave is stronger than that observed for the ONERA wing. Following the strong shock wave, there is a massive separation of the flow and this flow reattaches only at about the trailing edge of the wing. Also, the shock wave extends to the root of the wing as before. The shock gets weaker towards the tip region and the flow stays attached in this region. Figure 21 shows the surface oil flow pattern for this wing. The lines of separation, reattachment and other important flow features are delineated in this figure. Figure 22 shows the far-field view of the tip vortex for this wing. Also shown in this are the vorticity contours in the Y-Z plane at several X-locations of the tip vortex behind the wing. In contrast to the swept-tip ONERA wing, the tip vortex for this straight- and tapered-tip wing does not lift off the surface of the wing until after it passes the trailing edge of the wing tip.

The nondimensional tip vortex strength determined from integrating the velocity vector around a closed path surrounding the vortex yields a value of 0.17 when the path of integral includes the vortex sheet of the wake and a value of 0.21 for the path excluding most of the wake vortex sheet. This suggests a tip vortex strength of about 0.21.

Conclusions

A multi block zonal algorithm for solving the Euler and the Navier-Stokes equations is used to numerically simulate the formation and roll-up of the tip vortices of wings in subsonic and transonic flows. In all, four different wing geometries have been used as test cases. The influence of the tip-planform, the tip-cap shape, and the free-stream Mach number on the formation process has been studied. The numerical results from the TNS code agreed very well with the results from a single-block PEN3D code. Typical CPU run-time for each steady-state solution was about 3 hours on the CRAY-XMP machine.

Comparison of the numerical results with the limited available experimental data for both the subsonic and the transonic conditions shows good agreement for the surface pressures, except in the immediate vicinity of the tip, and for the tip vortex strength, where available. The disagreement of surface pressure distributions in the tip region is attributed to inadequate capability of predicting the shock-induced boundary-layer separation in the transonic cases. The subsonic calculations reproduce the qualitative behavior of the experimental tip vortex formation, including the changes in the tip separation and in the vortex lift off that have been observed experimentally and which have been caused by rounded tip-caps. However, the square-tip simulations fail to produce the correct suction peaks under the vortex. This may be due to an unrealistic sharp corner that was created at the tip leading edge by the H-H grid topology. Nevertheless, it has been demonstrated that it is possible to calculate the initial development of the tip vortex. The limited study presented here on the tip-cap effect on the flow field near the tip region suggests that the tip shape is an important ingredient of the problem.

As expected, the formation of the tip vortex involves braiding of the particle paths in the tip region from both the upper and lower surfaces of the wing. For a lifting wing the particles from underneath the wing (high-pressure side) cross over the tip region on to the upper surface (low-pressure side) and modify the flow field in the tip region by the three-dimensional tip-relief action. The tip vortex first lifts off from the surface and then rolls-up and moves inboard of the tip, staying distinctly above the wake vortex sheet. Both tip-cap modification and the tip-planform change had similar influences in increasing the gross lift of the wing and hence of the tip vortex strength. In addition, the modification to the ONERA planform delayed the lift off of the tip vortex from the surface.

The results demonstrate that although there is still room for improvement, realistic three-dimensional calculations of viscous flows over wings and their associated tip vortex formation are now feasible. This computational fluid dynamics capability provides a new tool for analyzing and improving the aerodynamic characteristics of wings and other lifting surfaces.

Acknowledgements

The first author would like to acknowledge the support of this research by the U. S. Army Research Office under Contract DAAG29-85-C-0002. The authors would like to express their sincere thanks to the members of TNS Group and in particular to Drs. T. L. Holst and U. Kaynak for several useful discussions. All the graphics work presented here was generated using the PLOT3D graphics package developed by Dr. P. G. Buning of NASA Ames Research Center. ONERA wing coordinates were supplied by Drs. C. Tung and F. H. Schmitz of the U. S. Army Aeroflightdynamics Directorate at NASA Ames Research Center.

References

1. Donaldson, C. duP. and Bilanin, A. J., "Vortex Wakes of Conventional Aircraft", AGARD-AG-204, May 1975.

2. Donaldson, C. duP., Bilanin, A. J. and Crow, S. C., "Vortex Wakes of Large Aircraft", AIAA Professional Study Series, 1974.

3. Francis, M. S. and Kennedy, D. A., "Formation of a Trailing Vortex", Journal of Aircraft, Vol. 16, No. 3, Mar. 1979, pp. 148-154.

4. Rizzi A., Eriksson L.-E., Schmidt W. and Hitzel S., "Numerical simulation of the Euler Equations simulating Vortex Flows Around Wings", Paper 21, AGARD-CP-342, April 1983.

5. Mitcheltree, R. A., Margason, R. J. and Hassan, H. A., "Euler Equation Analysis of the Initial Roll-Up of Aircraft Wakes", AIAA Paper-86-0078, AIAA 24th Aerospace Sciences Meeting, Jan. 1986.

6. Mansour N. N., "Numerical Simulation of the Tip Vortex Off a Low-Aspect Ratio Wing at Transonic Speed", AIAA Journal, Vol. 23, No. 8, 1985, pp. 1143-1149.

7. Pulliam T. H. and Steger J. L., "Implicit Finite-Difference Simulations of Three-Dimensional Compressible Flow", AIAA Journal, Vol. 18, No. 2, Feb. 1980, pp. 159-167.

8. Holst T. L., Gundy K. L., Flores J., Chaderjian N. M., Kaynak U. and Thomas S. D., "Numerical Solution of Transonic Wing Flows Using an Euler Navier-Stokes Zonal Approach", AIAA Paper-85-1640, July 1985.

9. Flores J., "Convergence Acceleration for a Three-Dimensional Euler Navier- Stokes Zonal Approach", AIAA Paper-85-1495, July 1985.

10. Pulliam, T. H., "Euler and Thin-Layer Navier-Stokes Codes: ARC2D, ARC3D", Notes for the Computational Fluid Dynamics User's Workshop, The University of Tennessee Space Institute, Tullahoma, Tenn., Mar. 1984.

11. Kaynak, U., Holst, T., Cantwell, B. J. and Sorenson, R. L., "Numerical Simulation of Transonic Separated Flows over Low-Aspect Ratio Wings", AIAA Paper-86-0508, Jan. 1986.

12. Beam, R. and Warming, R. F., "An Implicit Finite-Difference Algorithm for Hyperbolic Systems in Conservation Law Form", Journal of Computational Physics, Vol. 22, Sept. 1976, pp. 87-110.

13. Pulliam, T. H. and Chaussee, D. S., "A Diagonal Form of an Implicit Appriximate-Factorization Algorithm", Journal of Computational Physics, Vol. 39, No. 2, Feb. 1981, pp. 347-363.

14. Srinivasan G. R., Chyu W. J. and Steger J. L., "Computation of Simple Three-Dimensional Wing-Vortex Interaction in Transonic Flow", AIAA Paper-81-1206, June 1981.

15. Edwards T. A., "Noniterative Three-Dimensional Grid Generation Using Parabolic Partial Differential Equations", AIAA Paper-85-0485, Jan. 1985.

16. Spivey, W. A. and Moorhouse, G. G., "New Insights into the Design of Swept-Tip Rotor Blades", 26th Annual National Forum of the American Helicopter Helicopter Society, Washington, D. C., June 1970.

17. Spivey, W. A., "A Study to Investigate the Aerodynamics of Rotor Blade Tip Shapes", Bell Helicopter Company Report No. 299-099-468, Jan. 1970.

18. Steger, J. L. and Chaussee, D. S., "Generation of Body-Fitted Coordinates Using Hperbolic Partial Differential Equations", SIAM J. Sci. Stat. Comput., Vol.1, No. 4, Dec. 1980, pp. 431-437.

19. Pan, D. and Pulliam, T. H., "The Computation of Steady 3-D Separated Flows over Aerodynamic Bodies at Incidence and Yaw", AIAA Paper-86-0109, Jan. 1986.

20. Chigier, N. A. and Corsiglia, V. R., "Tip Vortices - Velocity Distributions", NASA TM X-62,087, Sept. 1971.

21. Keener E. R., "Computational-Experimental Pressure Distributions on a Transonic Low-Aspect-Ratio Wing", AIAA Paper-84-2092, Aug. 1984.

22. Hinson, B. L. and Burdges, K. P., "Acquisition and Application of Transonic Wing and Far-Field Test Data for Three-Dimensional Computational Method Evaluation", Vol. Appendix B, Experimental Data, Lockheed Georgia Company, AFOSR-TR-80-0422, 1980.

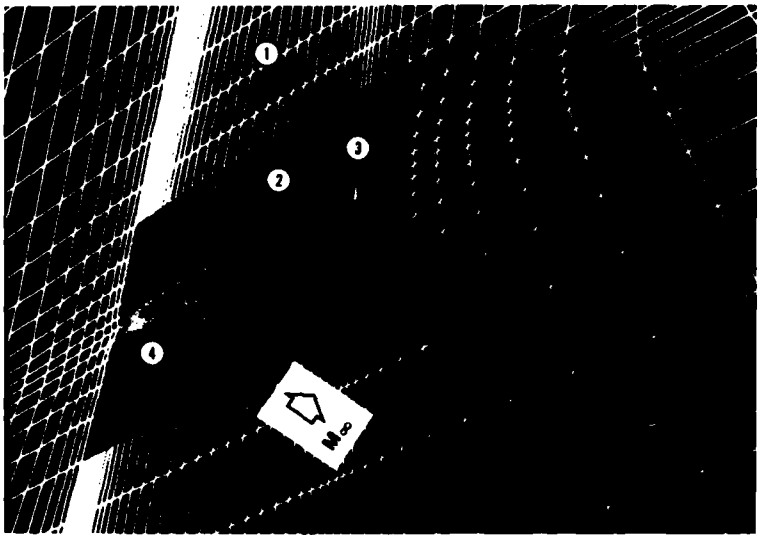

Fig. 1. Pictorial view of a typical zonal grid topology for the Wing C. Blocks 1 and 2 are inviscid zones and blocks 3 and 4 are viscous zones.

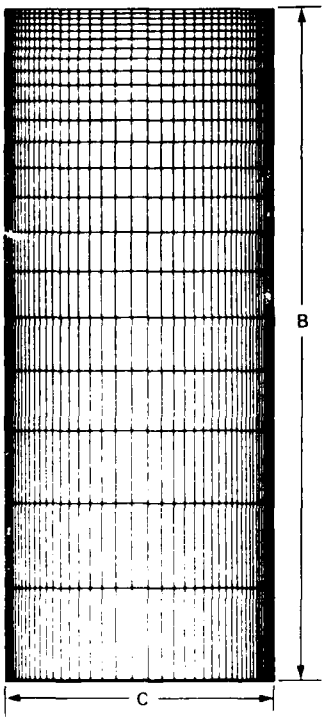

(a) NACA 0015
RECTANGULAR WING
B/C = 2.5

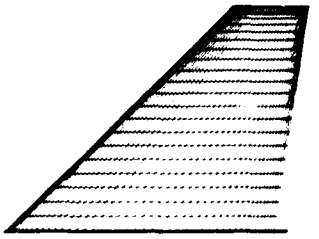

(b) WING C
B/C = 0.83

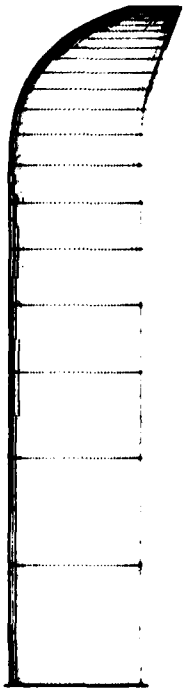

(c) ONERA WING
B/C = 5.0

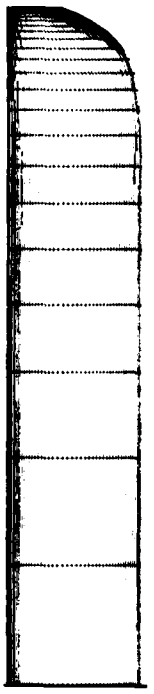

(d) MODIFIED
ONERA WING
B/C = 5.0

Fig. 2 Planform and surface grid of the four test wings.

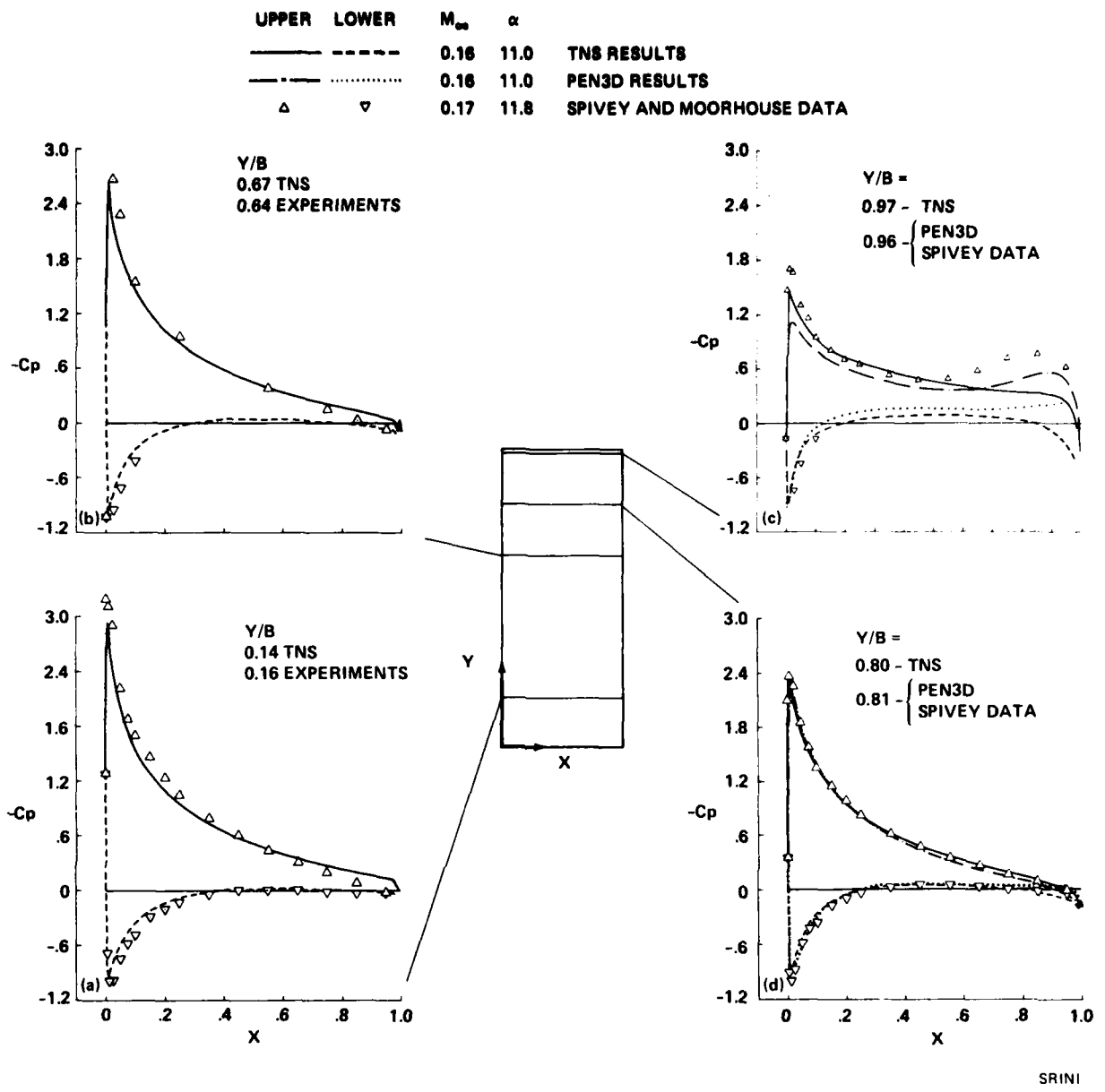

Fig. 3. Surface pressure distributions for several spanwise stations and comparison with experimental data (Refs. 16.17) for NACA 0015 wing. $M_\infty = 0.16$, $\alpha = 11$ degrees, and Re = 2 million.

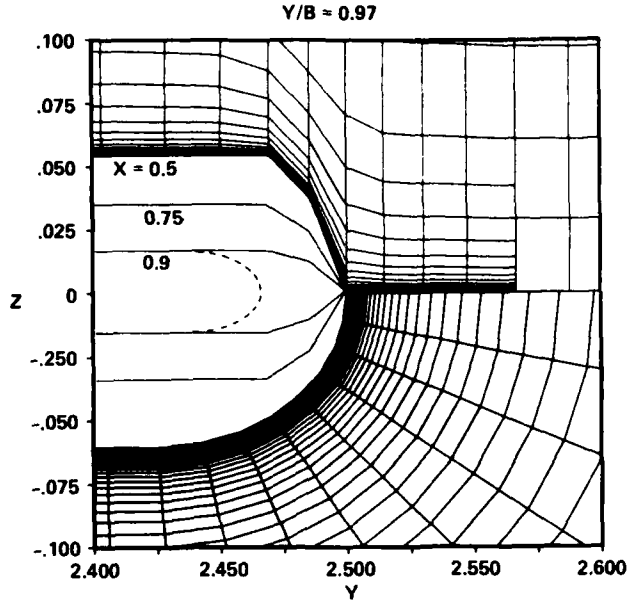

Fig. 4. Spanwise cross sectional views for NACA 0015 wing showing the details of tip-cap shapes at X = .5, .75 and .9. The associated grid for X = .5 station shows the grid-point distribution for the tip-cap.

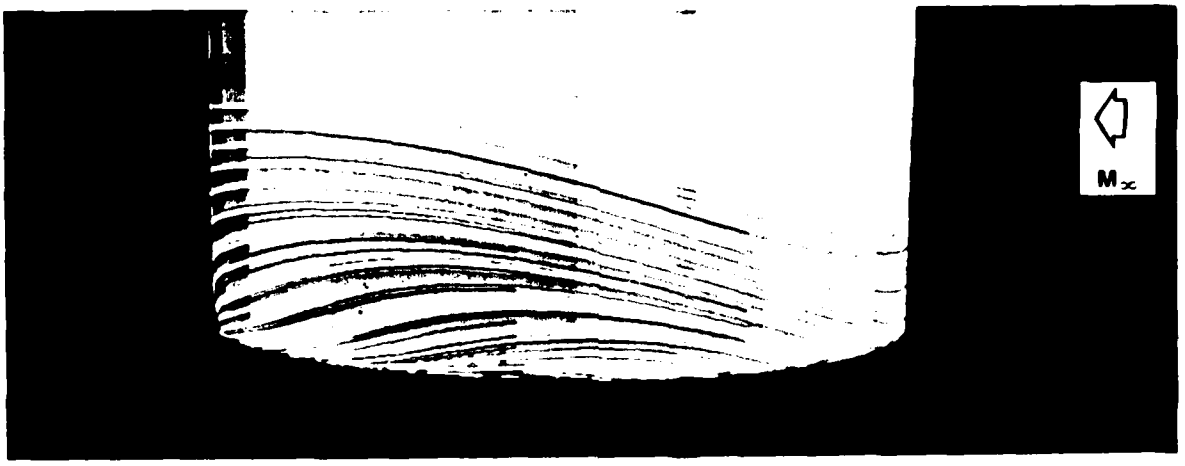

(a) SURFACE OIL FLOWS

(b) LIFT-OFF OF TIP VORTEX

Fig. 5. Close-up view of the surface oil flow pattern and the lift off of the tip vortex for the modified NACA 0015 wing with an ellipsiodal tip-cap. M_∞ = 0.16, α = 11 degrees, and Re = 2 million.

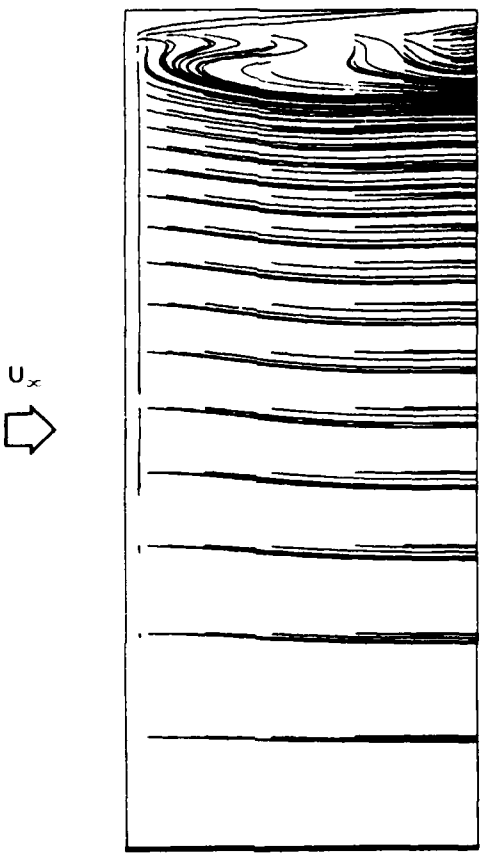

Fig. 6. Surface oil flow pattern for the rectangular NACA 0015 wing. $M_\infty = 0.16$, $\alpha = 11$ degrees, and Re = 2 million.

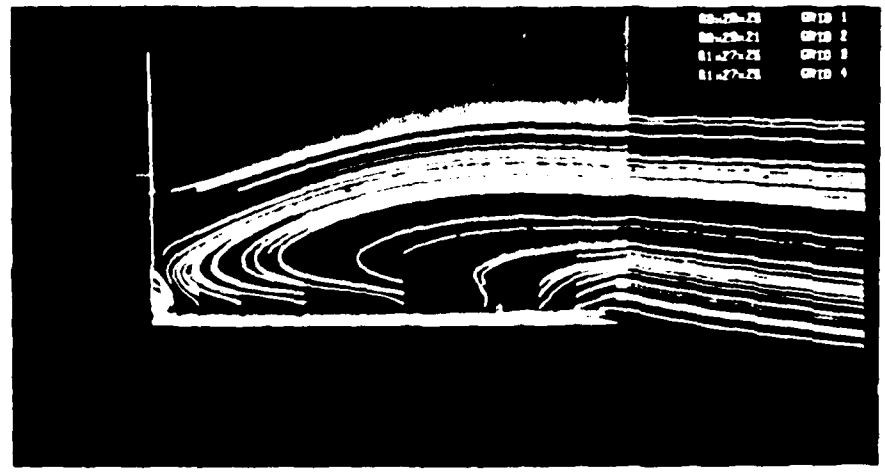

(a) SURFACE OIL FLOWS

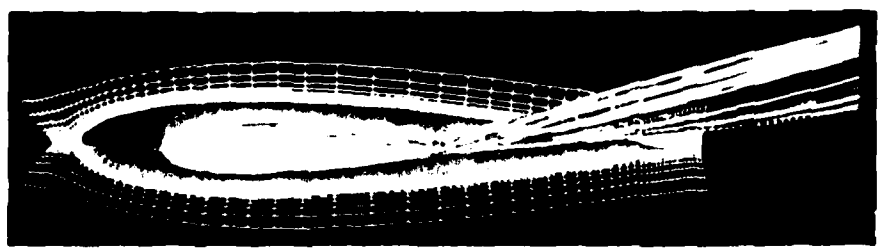

(b) LIFT OFF OF TIP VORTEX

Fig. 7. Close-up view of the surface oil pattern in the tip region and the lift off of the tip vortex for the NACA 0015 wing.

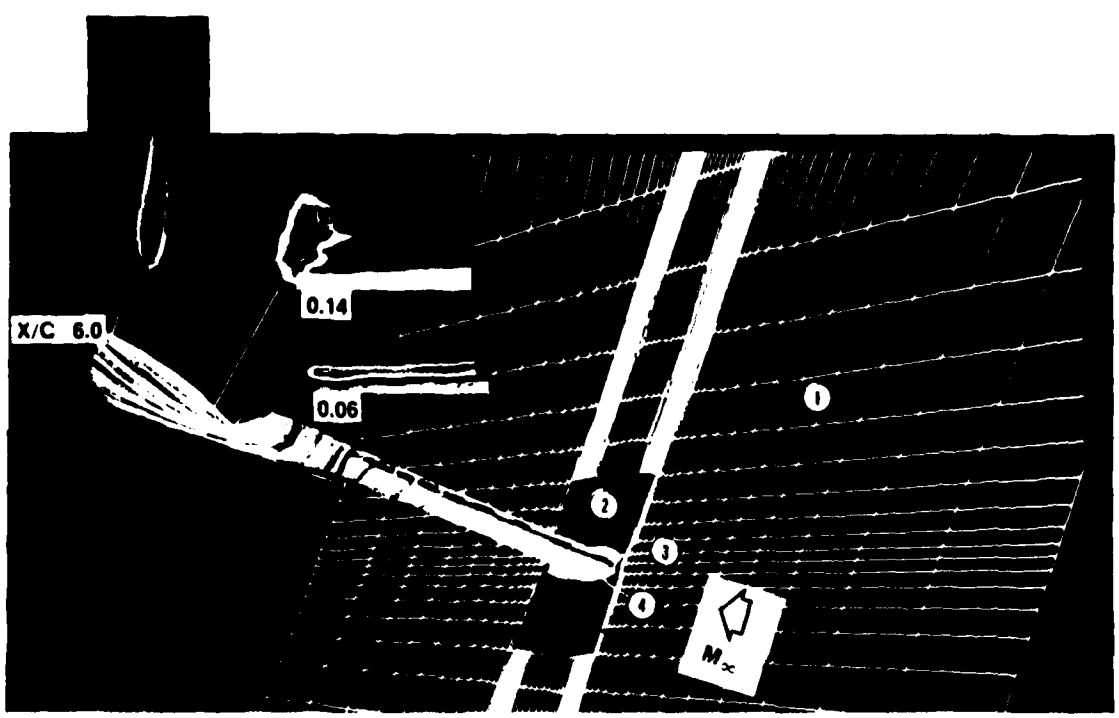

Fig. 8. Farfield view of the tip vortex for the NACA 0015 wing. The vorticity contours show the magnitudes and the shapes of the tip vortex at several X-stations.

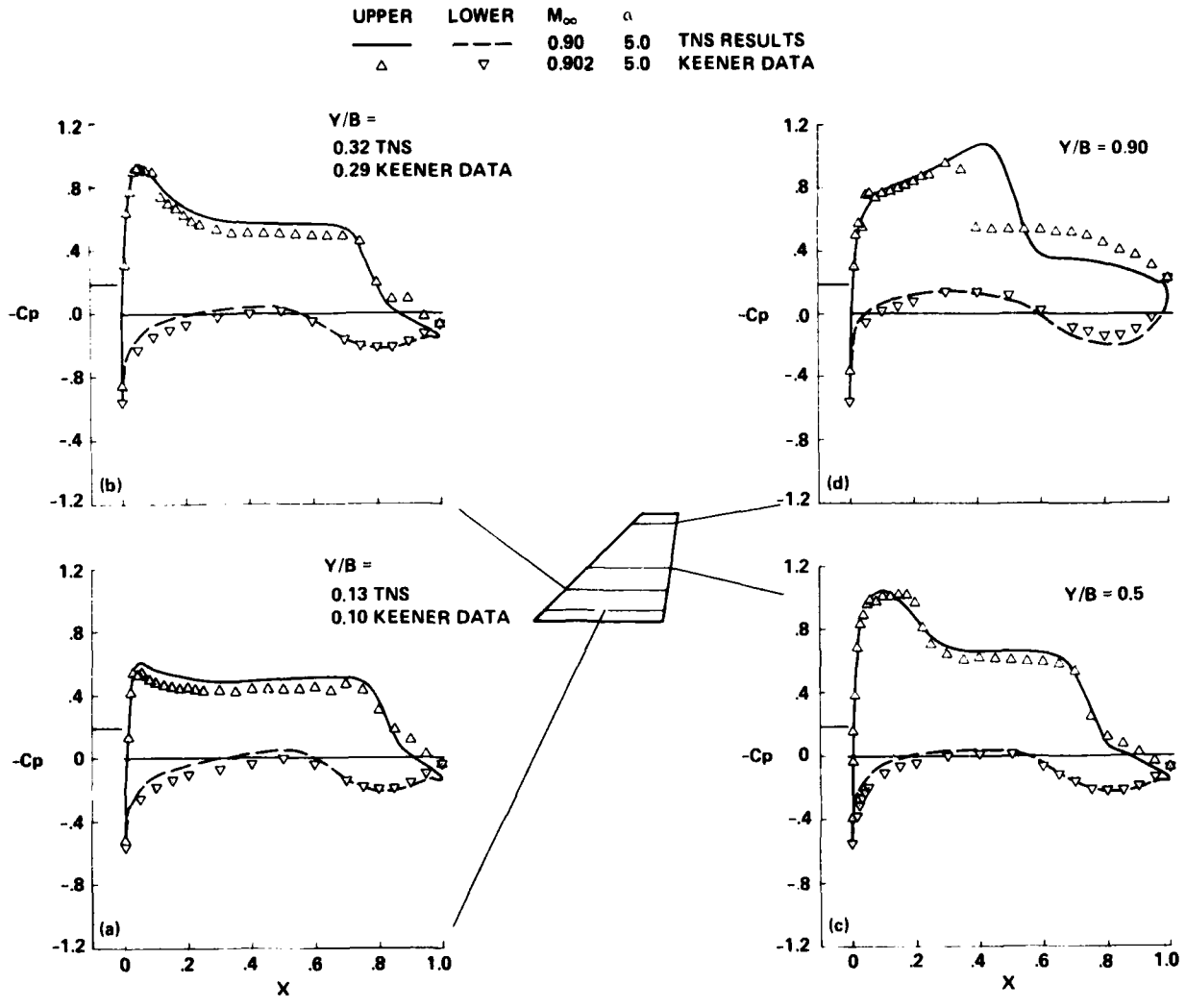

Fig. 9. Surface pressure distributions for several spanwise stations and comparison with experimental data (Ref. 21) for Wing C. $M_\infty = 0.90$, $\alpha = 5$ degrees, and Re = 6.8 million.

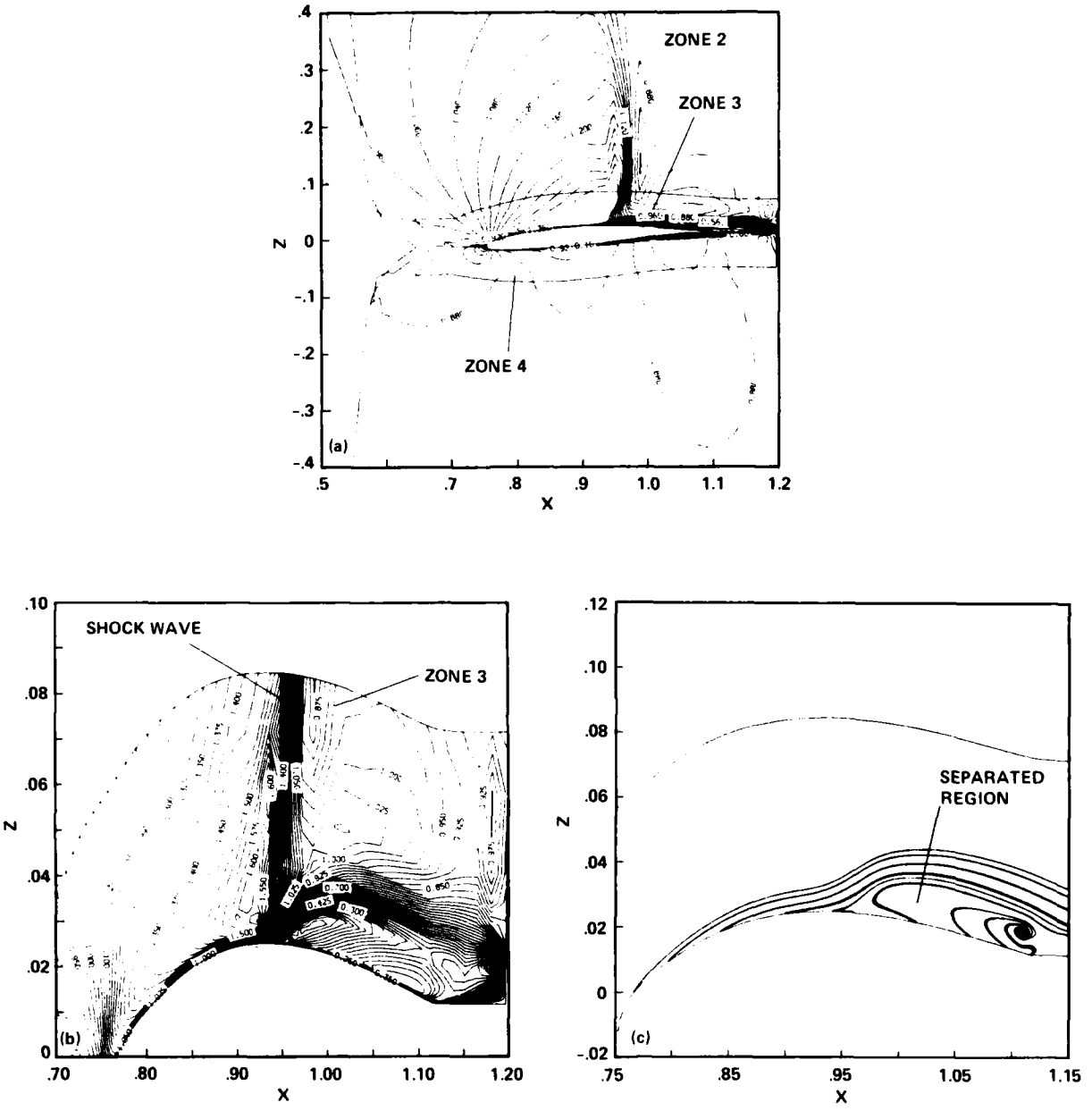

Fig. 10. Mach number contours and the separated region for the Wing C at Y B 0.88 station.

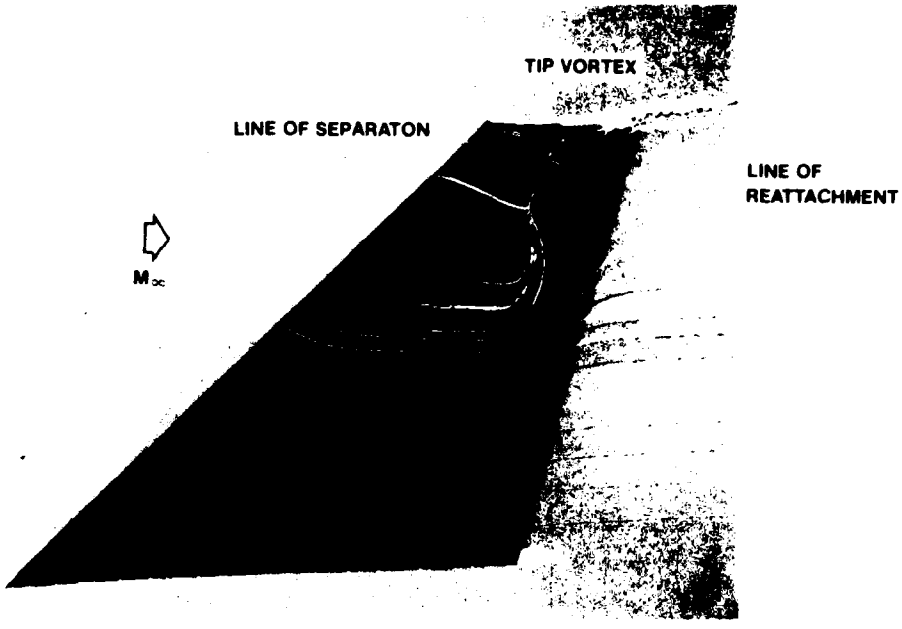

Fig. 11. Surface oil pattern showing separation and reattachment lines for the Wing C.

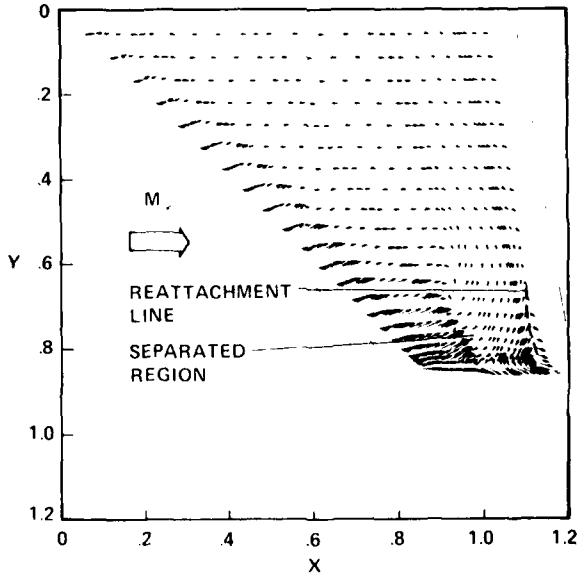

Fig. 12. Velocity vector plot for the upper surface of Wing C drawn at the first grid point above the surface.

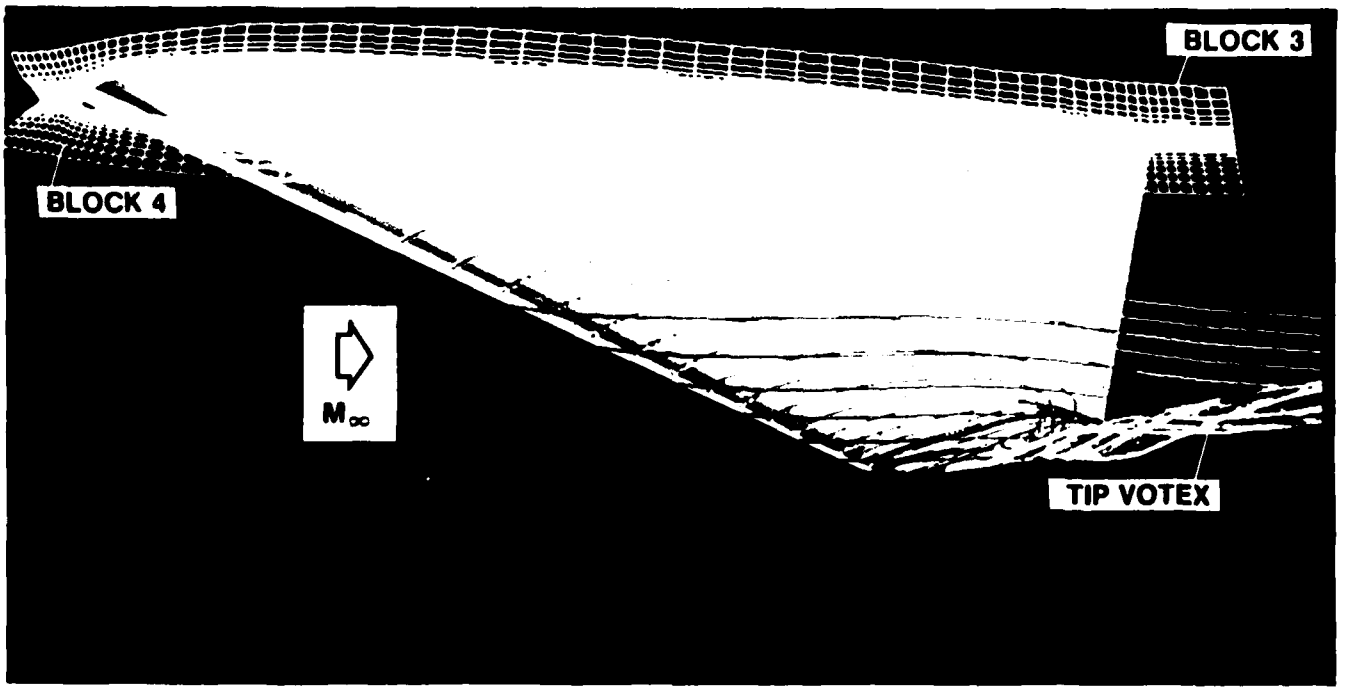

Fig. 13. Close-up view of the tip vortex for Wing C.

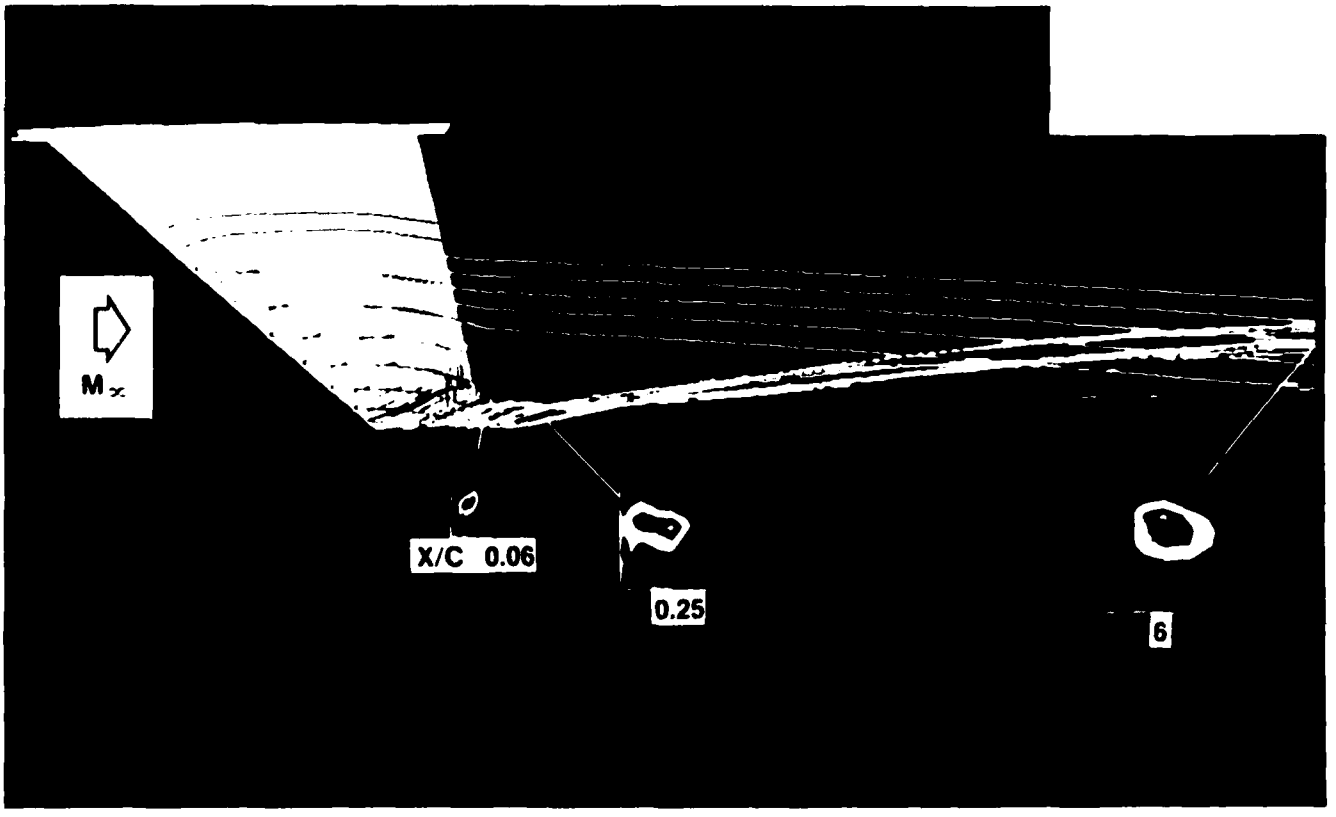

Fig. 14. Farfield view of the tip vortex for Wing C. The vorticity countours show the magnitudes and the shapes of the tip vortex at several X-stations.

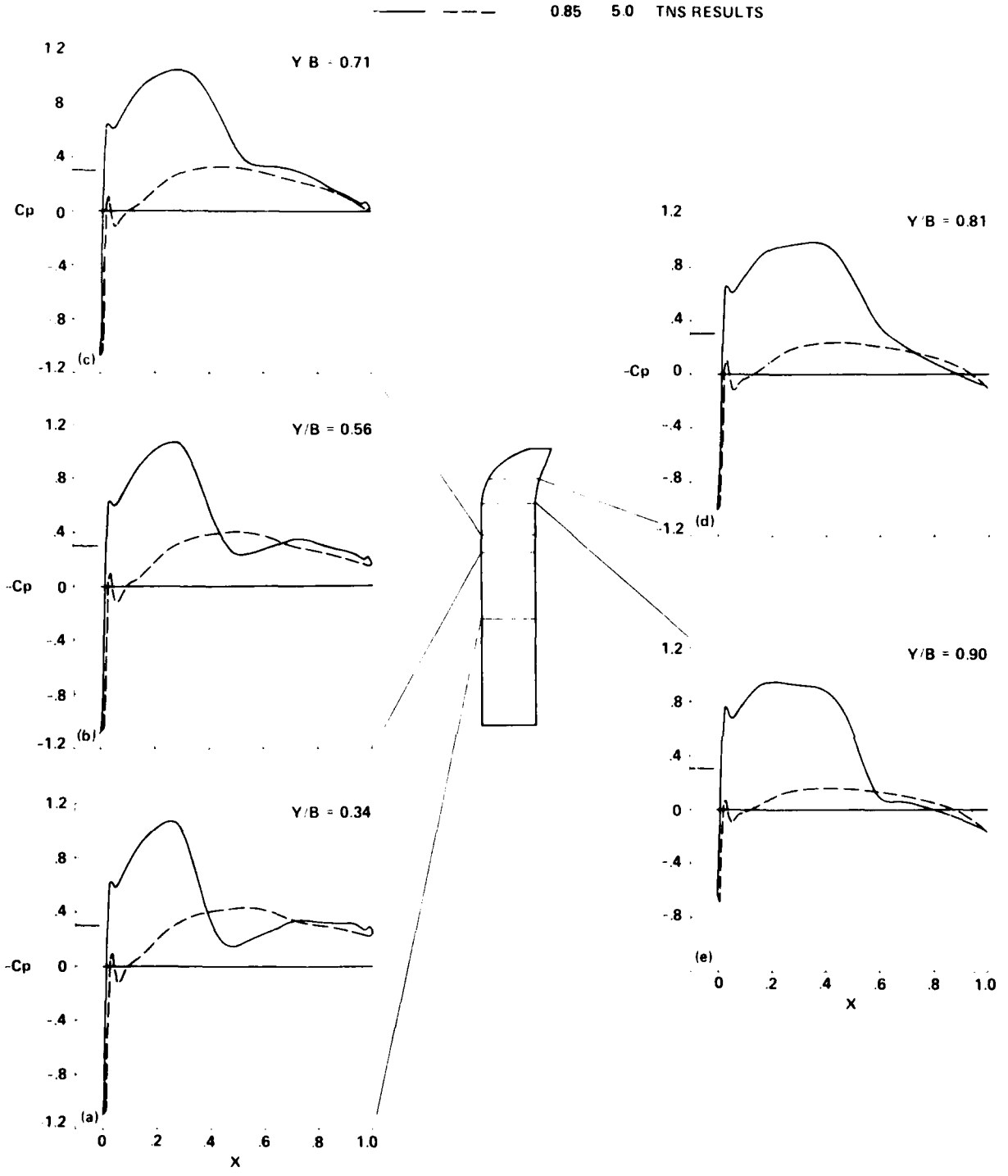

Fig. 15. Surface pressure distributions for the ONERA wing, M_∞ = 0.85, α = 5 degrees, and Re = 8.5 million.

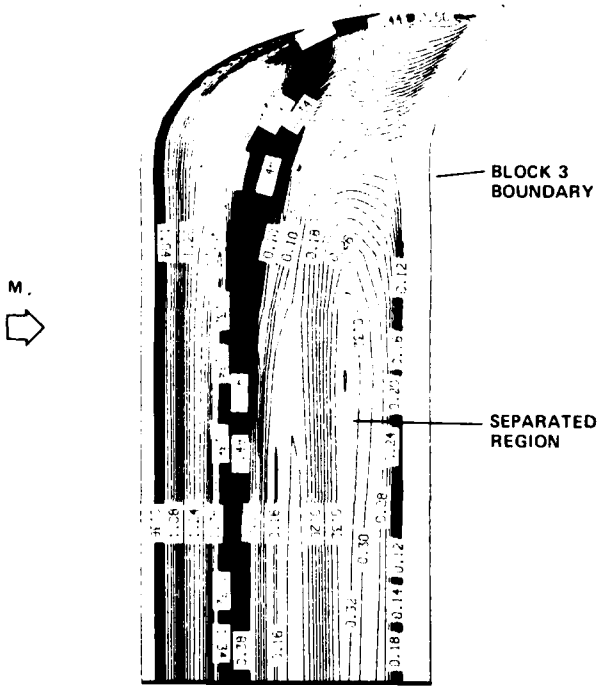

Fig. 16. Planform view of the upper surface Mach number contours for the ONERA wing.

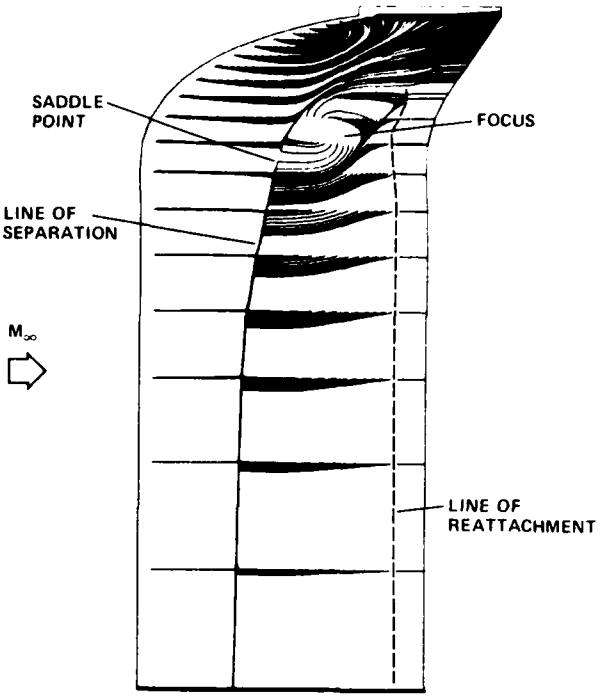

Fig. 17. Surface oil flow pattern for ONERA wing showing separation and reattachment lines.

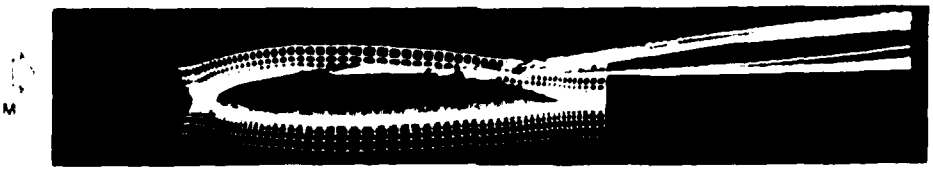

(a) TIP VORTEX LOOKING AT THE TIP

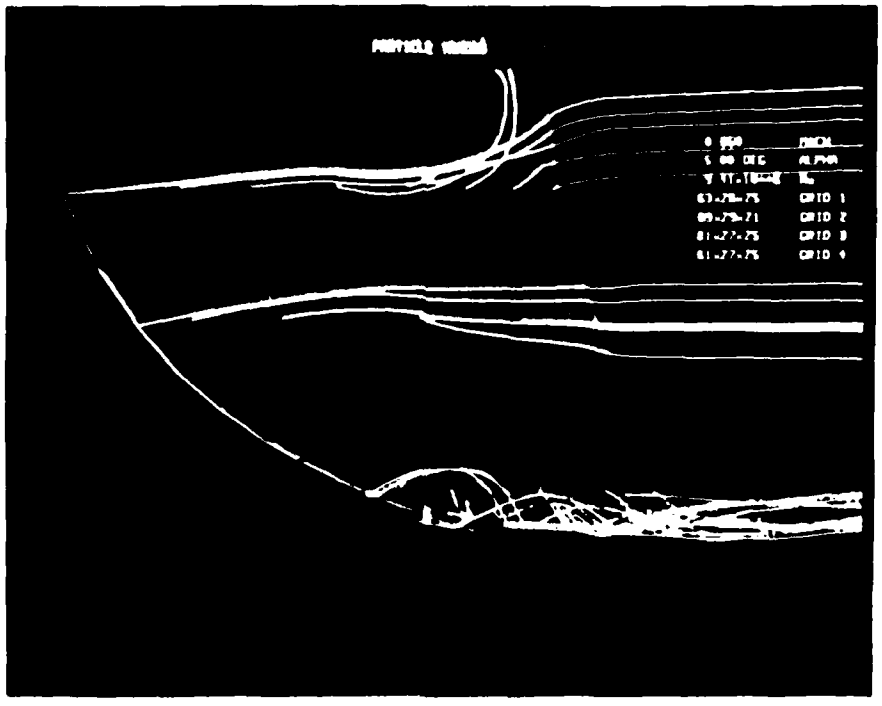

(b) ROLL-UP OF TIP VORTEX

Fig. 18. Close-up views of the lift off and roll-up of the tip vortex for the ONERA wing.

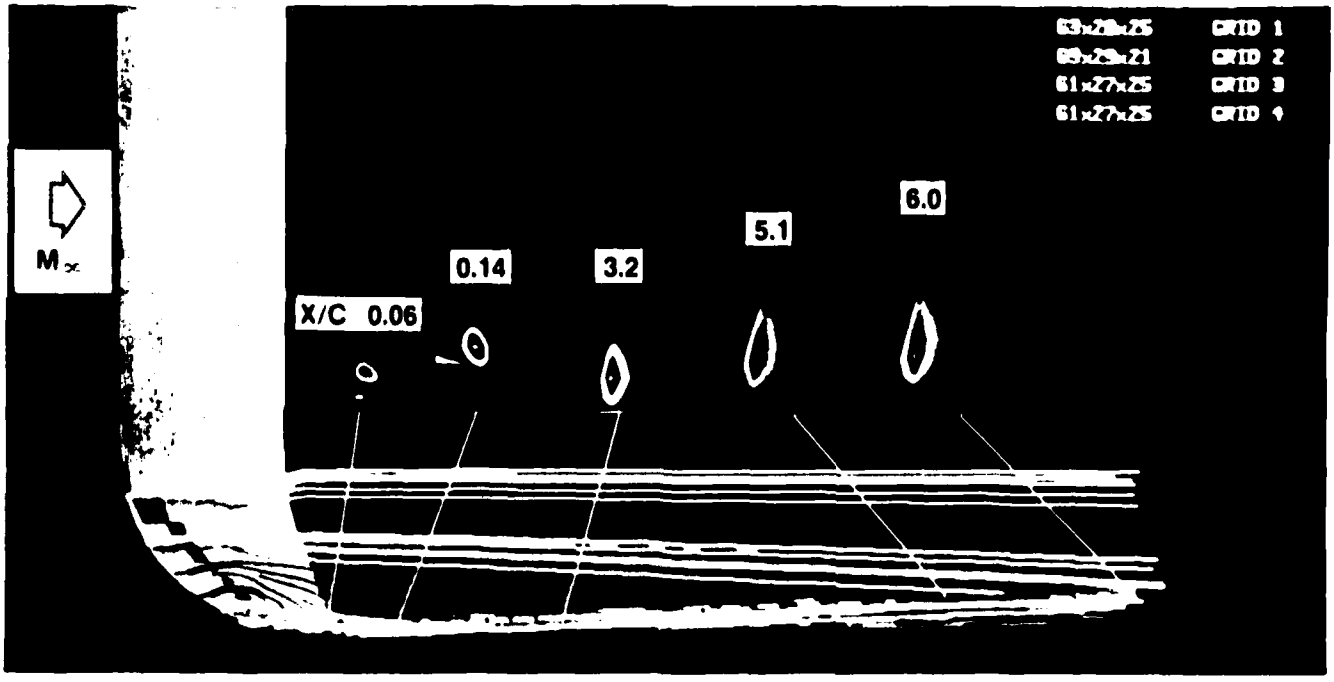

Fig. 19. Farfield view of the tip vortex for the ONERA wing. The vorticity contours show the magnitudes and the shapes of the tip vortex at several X-stations.

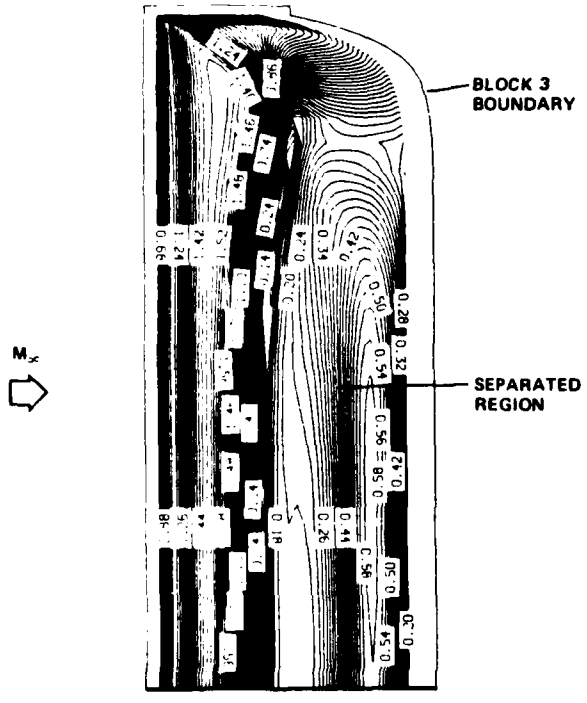

Fig. 20. Planform view of the upper surface Mach number contours for the modified ONERA wing. $M_\infty = 0.85$, $\alpha = 5$ degrees, and Re = 8.5 million.

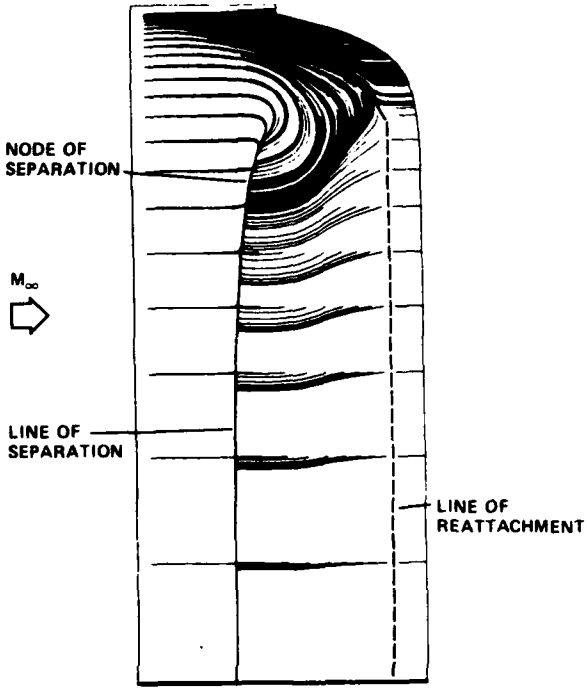

Fig. 21. Surface oil flow pattern for the modified ONERA wing showing the separation and reattachment lines.

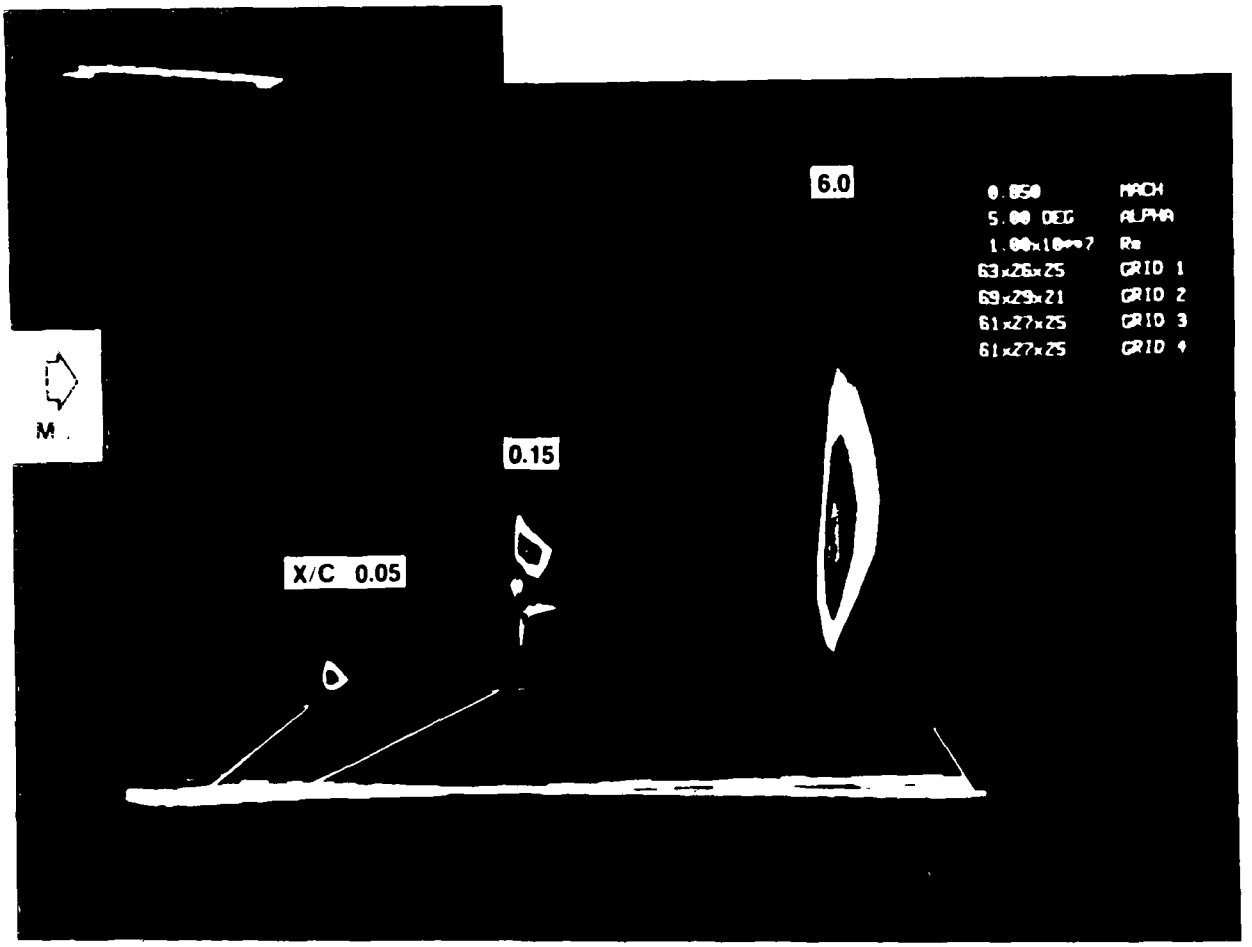

Fig. 22. Farfield view of the tip vortex for the modified wing. The vorticity contours show the magnitudes and the shapes of the tip vortex at several X-stations.

END

DTIC

7-86